

# Scaling Law Breaking in Unequal-size Droplet Coalescence

Xi Xia,<sup>1,\*</sup> Yicheng Chi,<sup>2,3,\*</sup> and Peng Zhang<sup>3,†</sup>

<sup>1</sup> School of Mechanical Engineering, Shanghai Jiao Tong University, Shanghai 200240, P. R. China

<sup>2</sup> School of Automotive and Transportation Engineering,

Shenzhen Polytechnic University, Shenzhen, Guangdong 518055, P. R. China

<sup>3</sup> Department of Mechanical Engineering, City University of Hong Kong, Kowloon Tong 999077, Hong Kong

This Letter examines the coalescence of two unequal-size spherical liquid droplets in the inviscid regime. We find that the liquid bridge evolution exhibits a breaking from the classical 1/2 power-law scaling [Phys. Rev. Lett. 95, 164503 (2005)]. Employing an energy balance analysis, we attain a theoretical model to collapse bridge evolution data of different droplet size ratios. This model reveals an exponential dependence of the bridge's radial growth on time, which is intrinsically scaling-free owing to the asymmetric movement of the liquid bridge.

PACS numbers:

In natural and industrial processes, the contact or impact of droplets [1–5] could lead to the coalescence of liquid-gas interfaces, which is crucial to the outcome or performance of the relevant applications. Extensive research has been carried out to understand the most basic situation, the momentumless coalescence of a pair of liquid droplets [6–9]. Early studies [1, 10] found that the radial growth of the liquid bridge, which forms between the merging droplets, satisfies certain scaling relations between the radius  $R$  of the bridge and time  $t$ . Later experimental [2, 6, 11–13] and numerical [14–17] works were able to confirm the existence of a 1/2 power-law scaling, i.e.  $R \sim \sqrt{t}$ , when the coalescence is in the inviscid (or inertial) regime. On the other hand, the bridge evolution in the viscous regime is better modeled by a linear scaling [2, 6, 7, 14, 18]. The crossover (or transition) [14] between the viscous and inertial regimes has also attracted considerable interest, from the discovery of a master curve for both regimes [7, 19] to the development of theoretical models justifying the underlying universality [20, 21].

Previous research on binary droplet coalescence mainly revolves around two equal-size droplets. However, less attention has been given to droplet coalescence with size disparities, despite its higher relevance to reality. Among the existing works involving the coalescence of unequal-size droplets [22–27], the main focus was on the effect of internal mixing facilitated by the break of symmetry. Regarding the evolution of the liquid bridge, it is evident from our previous work [27] that the bridge surface shows an asymmetric growth—the bridge interface becomes tilted as it expands out. Yet, little quantitative study exists on the liquid bridge evolution of unequal-size droplet coalescence.

In this Letter, we study the liquid bridge evolution for two unequal-size droplets merging in the inertial regime. We first conduct experiment to resolve the bridge's temporal variations for droplet pairs of various liquid properties and size ratios. Then, we develop a theory to model the radial growth of the liquid bridge, resulting in an ex-

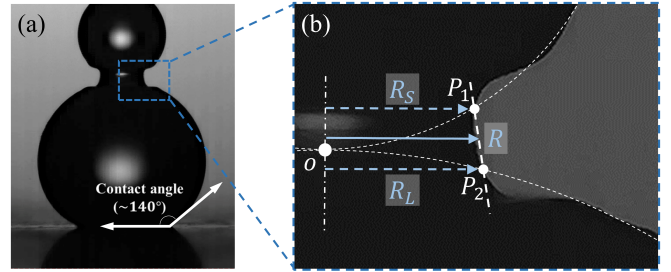


FIG. 1: (a) high-speed image of the sessile and pendant droplets and (b) zoomed-in detail of the liquid bridge.

ponential dependence of  $R$  on  $t$  that breaks the classical 1/2 power-law scaling relation.

*Experimental approach & observations.*—The present experiment employs the classical sessile-pendant approach for droplet coalescence, similar to those reported previously [2, 6, 12, 13]; see the Supplemental Materials [29] for a schematic of the setup. During each experimental run, a sessile droplet with a diameter of 1-5 mm is first generated by a syringe pump (Longer Precision Pump) and placed on a super-hydrophobic surface, yielding a contact angle of  $\sim 140^\circ$  and a near-spherical upper part as depicted in Fig. 1(a). Then, the syringe pump generates a smaller-size pendant droplet (1-2 mm in diameter), which is attached to the needle tip. Subsequently, the merging process is initiated by actuating an automatic lifting platform (Winner Optics) which holds the super-hydrophobic surface, slowly bringing the sessile droplet into contact with the pendant droplet. The platform rises at a speed about  $10 \mu\text{m/s}$ , which is sufficiently small to ignore the gas-film flow disturbing the initial droplet coalescence [7, 13, 28].

A high-speed camera (Photron SA-Z) integrated with a long-distance microscope (Questar QM100) is used to capture time-resolved shadowgraph images of the merging droplets. The camera operates at 150,000 frame per second (fps) with a spatial resolution of  $384 \times 256$  pixels and a field of view of  $2.04 \times 1.36 \text{ mm}^2$ , corresponding to a resolution of  $5.3 \mu\text{m}/\text{pixel}$ . The diameters of the

small and large droplets,  $D_S$  and  $D_L$ , are determined at the initial moment prior to the coalescence, based on fitting an arc to three arbitrarily-selected points on each droplet contour. The uncertainty associated with the diameter measurement is estimated to be within  $\pm 3\%$ . As such, the large-to-small droplet size ratio is defined as  $\Delta = D_L/D_S$ , which varies from 1.0 to 5.0 in the present experiment. Fig. 1(b) illustrates the zoomed-in detail of the liquid bridge, exhibiting a distinct asymmetric bridge interface. So two characteristic radii of the droplet bridge,  $R_S$  and  $R_L$ , can be respectively defined as the radial distances from the two points,  $P_1$  and  $P_2$ , where the bridge interface intersects the contours of the initial droplets (denoted by the white-dashed lines), to the axis of symmetry. Then, the characteristic radius of the circular bridge,  $R$ , is defined as  $R = (R_S + R_L)/2$ . Note this definition differs from the conventional one based on the minimum radial distance of the bridge interface to the center axis, so it yields a slightly larger  $R$ .

To study the effect of varying liquid properties, i.e., density  $\rho_l$ , dynamic viscosity  $\mu_l$ , and surface tension  $\sigma$ , we adopt water and two aqueous glycerol solutions with 40 wt% and 60 wt% glycerol. The three different liquids correspond to  $\rho = 1000$ , 1100, and 1150  $\text{kg}\cdot\text{m}^{-3}$ ,  $\mu = 1.002$ , 3.630, and 10.80  $\text{mPa}\cdot\text{s}$ , and  $\sigma = 72.8$ , 70.0, and 66.0  $\text{mN}\cdot\text{m}^{-1}$ , respectively. The Ohnesorge number, defined as  $Oh = \mu(\rho\sigma D_L)^{-1/2}$ , varies within  $10^{-3}$ - $10^{-2}$ . All cases are characterized in terms of  $\Delta$  and  $Oh$ , as summarized in the Supplemental Materials [29].

The image sequences for representative droplet coalescence cases are presented in Fig. 2(a-c), based on which the droplet interface contours corresponding to the different snapshots are extracted and overlapped in Fig. 2(b-f). It is seen that the liquid bridge displays a notable asymmetry for  $\Delta > 1$ , rendering an inclined bridge interface with  $R_L > R_S$ , which becomes increasingly evident as the bridge evolves with time. As  $Oh$  increases from 0.0016 to 0.0051, the bridge profiles in Fig. 2(f) follow the original droplet contour more closely than those in Fig. 2(e), as the secondary deformation on the bridge's upper and lower surfaces tends to be inhibited. This can be interpreted that the primary bridge movement gives rise to the development of a capillary wave along the droplet surface, which can be damped by enhanced viscosity. The experimental images for other cases can be found in the Supplemental Materials [29].

*Geometric correlations.*—Inspired by the liquid bridge configuration observed from the experiment, we present a geometric model for the bridge surface between two unequal-size droplets in Fig. 3, based on the core geometric variables of  $R_S(t)$ ,  $R_L(t)$ ,  $\theta_S(t)$ ,  $\theta_L(t)$ , and  $S(t)$ . In obtaining the geometric correlations, we consider the following conditions.

(i) ‘Similar-size droplets’, meaning the two droplets are of similar sizes such that  $\Delta \sim O(1)$ ,  $R_L/R_S \sim O(1)$ , and  $\theta_L/\theta_S \sim O(1)$ .

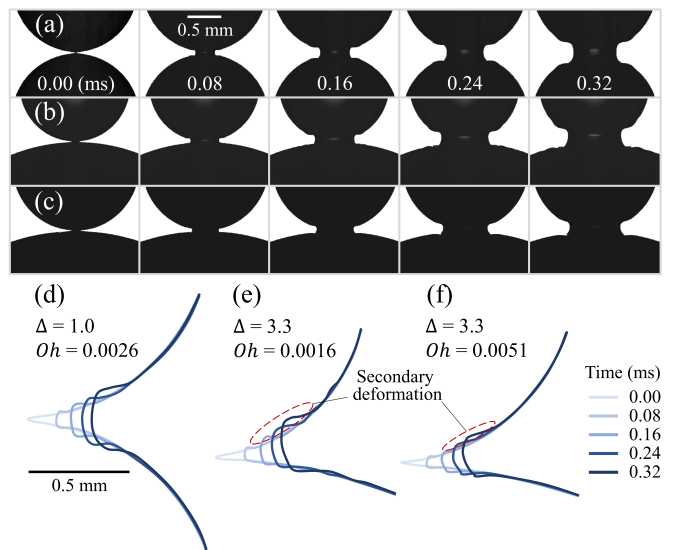


FIG. 2: Image sequences of the coalescence process of (a) equal-size water droplets and (b-c) unequal-size droplets of water and 40 wt% aqueous glycerol. (d-f) show the evolutions of the extracted interface contours corresponding to (a-c).

(ii) ‘Small bridge’, meaning that the characteristic radii of the bridge,  $R_S$  and  $R_L$ , are much smaller than the droplet diameters, i.e.,  $R_S/D_S \sim o(1)$  and  $R_L/D_L \sim o(1)$ . This condition is readily satisfied during the early-stage coalescence.

(iii) ‘Equally-dividable bridge interface’, meaning there exists a principle normal direction  $\mathbf{n}_p$  dividing the bridge interface into similar-shaped upper and lower sections, and the surface stress (including both pressure difference  $\Delta p$  and viscous stress  $\tau$ ) is also equally distributed over the two sections. Given the present experimental results, this condition can be considered a first approximation, although the two sections divided by  $\mathbf{n}_p$  might not be perfectly equal.

Based on Fig. 3, we can obtain the following geometric correlations,

$$\begin{aligned} \frac{R_S}{D_S} &= \frac{\sin(2\theta_S)}{2} = \theta_S - O(\theta_S^3), \\ \frac{R_L}{D_L} &= \frac{\sin(2\theta_L)}{2} = \theta_L - O(\theta_L^3). \end{aligned} \quad (1)$$

Applying condition (ii), it is deduced that both  $\theta_S$  and  $\theta_L$  are of  $o(1)$ ,  $\theta_S \approx R_S/D_S$ , and  $\theta_L \approx R_L/D_L$ . It follows that the width of the bridge,  $S$ , defined as the axial distance between  $P_1$  and  $P_2$ , satisfies

$$\begin{aligned} S &= R_S \tan \theta_S + R_L \tan \theta_L \\ &= R_S \theta_S + R_L \theta_L + R_S O(\theta_S^3) + R_L O(\theta_L^3). \end{aligned} \quad (2)$$

Combining Eqs. 1 and 2, we can easily show that  $S/D_S$  and  $S/D_L$  are of  $O(\theta_S^2)$  or  $O(\theta_L^2)$ .

Note that, compared with the equal-size situation, the unequal-size coalescence is characterized by the tilted

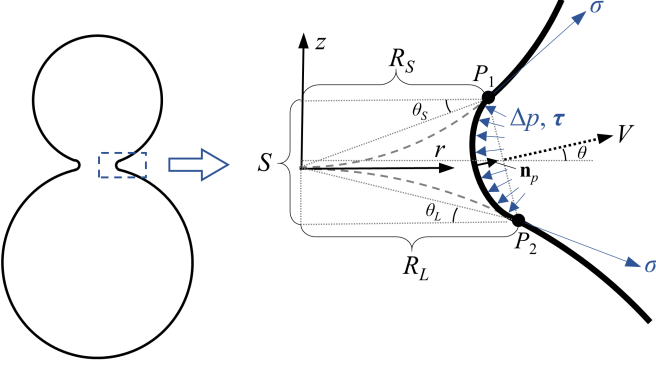


FIG. 3: Schematic of the liquid bridge between two unequal-size merging droplets.

bridge interface and the misaligned bridge movement from the radial direction, as illustrated in Fig. 3. The cause of the tilted interface may be understood in a force balance analysis. Under condition (iii), the principle normal direction  $\mathbf{n}_p$  of the bridge interface should align with the integral of the total surface stress across the interface, which is balanced by the surface tension exerted at both ends of the bridge interface. Given the two surface tension forces are identical to each other,  $\mathbf{n}_p$  must be in line with the angular bisector of the two surface tension forces. Therefore, the tilting angle of the bridge interface,  $\theta$ , can be simply expressed as

$$\theta = \theta_S - \theta_L. \quad (3)$$

Since both  $\theta_S$  and  $\theta_L \sim o(1)$ , Eq. 3 implies that  $\theta$  is also a  $o(1)$  quantity. Thus,  $\theta$  is treated as the ‘small parameter’ hereinafter. From Fig. 3, we further note another geometric relationship,  $R_L - R_S = S \tan \theta \approx S\theta$ , which can be combined with Eqs. 1 and 3 to yield

$$\begin{aligned} \theta &\approx \left( \frac{1}{D_S} - \frac{1}{D_L} \right) R - \left( \frac{1}{D_S} + \frac{1}{D_L} \right) \frac{S\theta}{2} \\ &\approx \left( \frac{1}{D_S} - \frac{1}{D_L} \right) R. \end{aligned} \quad (4)$$

The second term on the right-hand side of Eq. 4 is negligible compared with  $\theta$  because  $S/D_S \sim O(\theta_S^2)$  and  $S/D_L \sim O(\theta_L^2)$ , as indicated from Eq. 2. Similarly, we can apply  $R_L - R_S \approx S\theta$  to Eqs. 1 and 2 to obtain

$$\begin{aligned} S &\approx \left( \frac{1}{D_S} + \frac{1}{D_L} \right) R^2 + \left( \frac{R_L + R}{D_L} - \frac{R_S + R}{D_S} \right) \frac{S\theta}{2} \\ &\approx \left( \frac{1}{D_S} + \frac{1}{D_L} \right) R^2. \end{aligned} \quad (5)$$

Again, the second term on the right-hand side of Eq. 5 is dropped out because it is a  $O(\theta^2)S$  term.

On the other hand, given the equally-distributed viscous stress,  $\tau = 2\mu\mathbf{S}$  with  $\mathbf{S}$  being the strain-rate tensor, the liquid-side velocity must also be equally distributed over the bridge interface, so the overall bridge movement

also points in the direction of  $\mathbf{n}_p$ . The physical implication here is significant. Consider the very early stage of coalescence when  $R_S \approx R_L$ , Eq. 3 dictates that  $\theta$  is a positive value, which explains why the bridge movement is inclined towards the smaller droplet from the beginning. It follows that the velocity  $V$  at which the bridge interface expands out is given by the kinematic relationship,  $dR/dt = V \cos \theta$ . After Taylor expansion, it takes the form

$$\frac{dR}{dt} \approx V \left( 1 - \frac{\theta^2}{2} \right). \quad (6)$$

*Energy balance analysis and solution.*—Now, considering the energy balance during the coalescence process, the movement of the liquid entrained by the bridge is driven by the rapid discharge of the surface energy, which can be expressed as

$$\Delta E_s + \Delta E_k \approx 0, \quad (7)$$

where  $\Delta E_s$  and  $\Delta E_k$  represent the changes in surface and kinetic energies, respectively, from the initial state before coalescence. Note Eq. 7 requires the viscous dissipation being negligible compared to the change in inertia energy. Based on the geometries in Fig. 3, we have

$$\begin{aligned} \Delta E_s &= -\pi D_S^2 (\theta_S^2 + O(\theta_S^4)) \sigma - \pi D_L^2 (\theta_L^2 + O(\theta_L^4)) \sigma \\ &\quad + \pi S (R_S + R_L) [1 + O((\theta_S + \theta_L)^2)] \sigma, \end{aligned} \quad (8)$$

where  $\sigma$  is the surface tension. Since  $\theta_S$  and  $\theta_L \sim o(1)$ , we can combine Eqs. 1 and 2 to obtain  $S \approx R_S \theta_S + R_L \theta_L \approx D_S \theta_S^2 + D_L \theta_L^2$ . Thus, the third term on the right-hand side of Eq. 8 has the leading order of  $O(\theta_S^3) D_S^2 \sigma$  or  $O(\theta_L^3) D_L^2 \sigma$ , which is one order smaller than the first two terms and can be dropped out. Next,  $\Delta E_k$  can be estimated as

$$\Delta E_k \approx \frac{C}{2} \pi \rho_l R^2 S V^2, \quad (9)$$

where  $\rho_l$  is the liquid density and  $C$  is a prefactor related to the volume and velocity distribution of the moving fluid entrained with the bridge.

With  $S$  given by Eq. 5, we can plug Eqs. 8 and 9 into Eq. 7 and balance the leading order terms to obtain

$$\frac{C}{2} \rho_l R^4 \left( \frac{1}{D_S} + \frac{1}{D_L} \right) V^2 \approx 2R^2 \sigma. \quad (10)$$

Further substituting  $V$  using Eqs. 6 and 4, we have

$$\frac{1}{1 - \beta R^2/2} \frac{dR}{dt} \approx \frac{\gamma}{R}. \quad (11)$$

In simplifying Eq. 11, we define  $\beta$  and  $\gamma$  as

$$\beta = \left( \frac{1}{D_S} - \frac{1}{D_L} \right)^2 \quad \text{and} \quad \gamma = \left[ \frac{4\sigma D_S}{C \rho_l (1 + 1/\Delta)} \right]^{1/2}. \quad (12)$$

Eq. 11 has the solution:

$$R^2 \sim \frac{1 - e^{-\beta\gamma t}}{\beta}, \quad (13)$$

where the initial condition,  $R(t=0) = 0$ , has been used in the derivation. Eq. 13 can further take the nondimensional form of

$$R^{*2} \sim 1 - e^{-t^*}, \quad (14)$$

where  $R^* = R\beta^{1/2}$  and  $t^* = t\beta\gamma$ . Interestingly, the bridge evolution governed by Eq. 13 or 14 no longer has a power-law scaling between  $R$  and  $t$ . However, by letting  $\Delta \rightarrow 1$ , we have  $\beta \rightarrow 0$  and  $R^2 \sim [1 - (1 - \beta\gamma t)]/\beta = \gamma t$ . This means that the present model is able to recover the inviscid scaling law of  $R \sim t^{1/2}$  in the equal-size limit.

*Discussion.*—It is worth discussing the origin of this scaling-free solution. Mathematically, the exponential dependence of  $R$  on  $t$  arises from the  $\theta^2$  term in Eq. 6. If  $\theta = 0$  is set in Eq. 6, the above analysis would give the exact scaling relation of  $R \sim t^{1/2}$ . Thus, we can infer that the breaking of the power-law scaling results from the misaligned movement of the liquid bridge from the radial direction.

Next, we check the scaling breaking behavior for the present experimental data of various  $\Delta$  and  $Oh$ . In Fig. 4, the classical scaling law of  $R \sim t^{1/2}$  is evaluated by plotting the data in the parameter space  $[(8\sigma/\rho D_S^3)^{1/2}t, (2R/D_S)^2]$  [2, 10]. While the overall scaling of  $R^2 \sim t$  is still valid for most cases, there is an apparent upward drift of large- $\Delta$  data. And a larger  $\Delta$  tends to cause a larger shift from the  $\Delta = 1.0$  line. This can be understood that the presence of a larger droplet enhances the expansion speed of the bridge interface, corresponding to a larger prefactor of the power-law scaling. Furthermore, the cases with  $\Delta > 3$  display a gradual deflection from  $R^2 \sim t$  as time proceeds and the liquid bridge becomes more asymmetric, indicating a diversion from the power-law scaling.

To evaluate our theory, Fig. 5 shows the validation of Eq. 14 based on the same set of data in Fig. 4. We can confirm the collapse of non-unity- $\Delta$  data onto a single line given by Eq. 14 with  $C = 1.5$  ( $C$  is obtained by fitting Eq. 14 with a unity prefactor). Here, the effect of  $\Delta$  is assimilated into the time and length scales. In particular, a larger  $\Delta$  generally corresponds to higher  $R^*$ , as  $R$  is scaled by  $\beta^{-1/2}$  that is highly sensitive to  $\Delta$ . This result also demonstrates that the present model has a negligible dependence on viscosity for  $Oh$  varying between  $10^{-3}$  and  $10^{-2}$ . The theoretical line in Fig. 5 remains almost linear when  $R^{*2} < 10^{-1}$ , while it exhibits notable deflection or deviation from the power-law scaling when  $R^{*2} > 10^{-1}$ . Given the correlation between  $\Delta$  and  $R^*$ , this means that the scaling-law breaking is manifest when  $\Delta$  is greater than 3 or so, which explains the observed scaling diversion in Fig. 4.

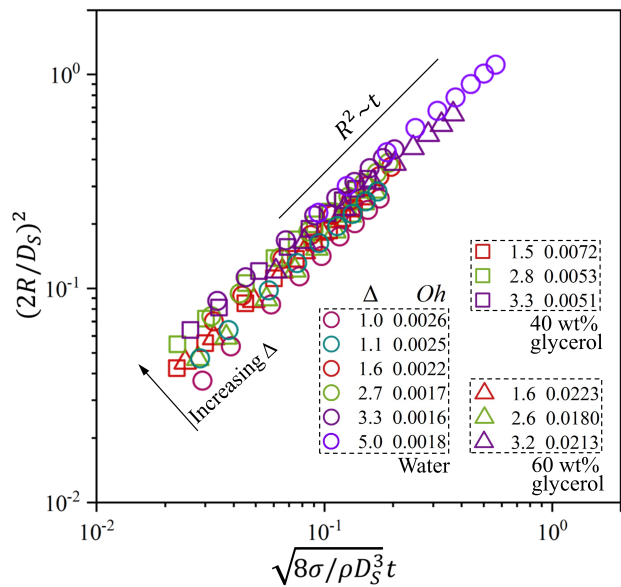


FIG. 4: Effect of  $\Delta$  on the scaling of  $R^2 \sim t$ . See Supplemental Materials [29] for detailed experimental parameters.

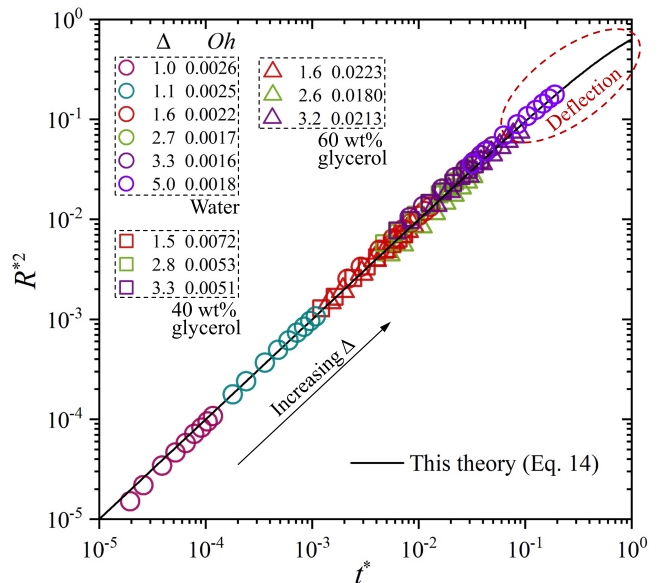


FIG. 5: Validation of Eq. 14 against experimental data.

In summary, this Letter reports the breaking of the  $1/2$  power-law scaling for the liquid bridge evolution during the coalescence of unequal-size droplets. By accounting for the asymmetric motion of the liquid bridge interface, we attain a new solution for the bridge evolution in the inviscid regime based on balancing the changes in surface and kinetic energies. The derived model shows distinct scaling-free feature and well resolves the droplet coalescence of non-unity size ratios.

We acknowledge financial support from the National Natural Science Foundation of China (No. 52176134 and 12072194), the Research Grants Council of the Hong Kong Special Administrative Region, China (Project No.



CityU 15218820), and the APRC-CityU New Research Initiatives/Infrastructure Support from Central of City University of Hong Kong (No. 9610601). We thank Dr. Tao Yang and Jiayue Han for their assistance in data processing.

---

\* X.X. and Y.C. contributed equally to this work

† Electronic address: penzhang@cityu.edu.hk

- [1] J. Eggers, J. R. Lister, and H. A. Stone, *J. Fluid Mech.* **401**, 293 (1999).
- [2] D. G. A. L. Aarts, H. N. W. Lekkerkerker, H. Guo, G. H. Wegdam, and D. Bonn, *Phys. Rev. Lett.* **95**, 164503 (2005).
- [3] A. L. Yarin, *Ann. Rev. Fluid Mech.* **38**, 159 (2006).
- [4] M.-J. Thoraval, K. Takehara, T. G. Etoh, S. Popinet, P. Ray, C. Josserand, S. Zaleski, and S. T. Thoroddsen, *Phys. Rev. Lett.* **108**, 264506 (2012).
- [5] T. Tran, H. de Maleprade, C. Sun, and D. Lohse, *J. Fluid Mech.* **726**, R3 (2013).
- [6] S. T. Thoroddsen, K. Takehara, and T. G. Etoh, *J. Fluid Mech.* **527**, 85 (2005).
- [7] J. D. Paulsen, J. C. Burton, and S. R. Nagel, *Phys. Rev. Lett.* **106**, 114501 (2011).
- [8] P. Zhang and C. K. Law, *Phys. Fluids* **23**, 042102 (2011).
- [9] H. P. Kavehpour, *Ann. Rev. Fluid Mech.* **47**, 245 (2015).
- [10] L. Duchemin, J. Eggers, and C. Josserand, *J. Fluid Mech.* **487**, 167 (2003).
- [11] M. Wu, T. Cubaud, and C.-M. Ho, *Phys. Fluids* **16**, L51 (2004).
- [12] K. Fezzaa and Y. Wang, *Phys. Rev. Lett.* **100**, 104501 (2008).
- [13] S. C. Case, *Phys. Rev. E* **79**, 026307 (2009).
- [14] J. C. Burton and P. Taborek, *Phys. Rev. Lett.* **98**, 224502 (2007).
- [15] J. C. Pothier and L. J. Lewis, *Phys. Rev. B* **85**, 115447 (2012).
- [16] M. Gross, I. Steinbach, D. Raabe, and F. Varnik, *Phys. Fluids* **25**, 052101 (2013).
- [17] J. E. Sprittles and Y. D. Shikhmurzaev, *Phys. Fluids* **24**, 122105 (2012).
- [18] W. Yao, H. J. Maris, P. Pennington, and G. M. Seidel, *Phys. Rev. E* **71**, 016309 (2005).
- [19] J. D. Paulsen, *Phys. Rev. E* **88**, 063010 (2013).
- [20] X. Xia, C. He, and P. Zhang, *Proc. Natl. Acad. Sci. U.S.A.* **116**, 23467 (2019).
- [21] M. A. Hack, W. Tewes, Q. Xie, C. Datt, K. Harth, J. Harting, and J. H. Snoeijer, *Phys. Rev. Lett.* **124**, 194502 (2020).
- [22] A. V. Anilkumar, C. P. Lee, and T. G. Wang, *Phys. Fluids A* **3**, 2587 (1991).
- [23] F. Blanchette, *Phys. Rev. Lett.* **105**, 074501 (2010).
- [24] D. Liu, P. Zhang, C. K. Law, and Y. Guo, *Int. J. Heat Mass Transfer* **57**, 421 (2013).
- [25] K. Sun, T. Wang, P. Zhang, and C. K. Law, *Phys. Rev. E* **91**, 023009 (2015).
- [26] C. Tang, J. Zhao, P. Zhang, C. K. Law, and Z. Huang, *J. Fluid Mech.* **795**, 671 (2016).
- [27] X. Xia, C. He, D. Yu, J. Zhao, and P. Zhang, *Phys. Rev. Fluids* **2**, 113607 (2017).
- [28] S. C. Case and S. R. Nagel, *Phys. Rev. Lett.* **100**, 084503 (2008).
- [29] See Supplemental Materials for a parameter list of all experimental cases.